# Magnetic Resonance Imaging

G.A. WRIGHT

Nuclear magnetic resonance (NMR), a property of atoms first observed by Bloch [1] and Purcell [2] in 1946, has proven to be an informative technique in many fields of study, particularly in chemistry and physics. The magnetic resonance signal is very rich in measurable characteristics—including initial strength, frequency of oscillation, and rate of recovery and decay—that reflect the nature of a population of atoms, the structure of their environment, and the way in which the atoms interact with this environment. Furthermore, one can manipulate the external magnetic environment in space and time to modify the NMR signal without significantly affecting material structure.

Relatively recently, magnetic resonance was extended to the *in vivo* study of human anatomy. This was made possible by new, practical methods for exciting a signal from limited volumes [3] and for generating spatial maps of this signal [4]. Relying primarily on the differential decay and recovery characteristics of the proton NMR signal (generally termed relaxation behavior), this technology can generate images with high contrast among various soft tissues and organs. As a result, magnetic resonance imaging (MRI) has become the modality of choice in many diagnostic studies of the head, spine, and joints. With ongoing developments to improve the image quality, acquisition speed, and quantitative accuracy of related measures of local signal characteristics, the range of clinical applications for MRI continues to expand rapidly.

Signal processing lies at the core of MRI. Data acquisition and manipulation occur naturally in the spatial Fourier trans-
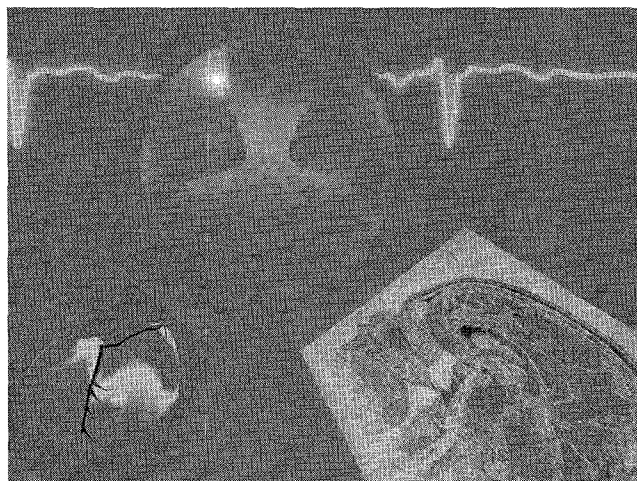
**From Basic Physics to Imaging Principles**

form domain of the image. A review of the imaging process and the associated image characteristics reveals the many opportunities for contributions from the signal processing community. This article develops the Fourier representation of the imaging process from an overview of the physics of the MRI signal. This article also discusses tradeoffs in acquisition time, resolution, and field of view as well as image degradation associated with noise and motion artifacts. In addition, the ability to manipulate soft tissue contrast over a wide range of independent parameters in MRI is outlined.

Basic Physics: The MR Signal

In almost all MRI applications, the signal originates from the hydrogen nucleus, which is a single proton. The relevant property of the proton is its spin, I, and a simple classical picture of spin is a charge distribution in the nucleus rotating around an axis collinear with I. The resulting current has an associated dipole magnetic moment, μ, collinear with I, and the quantum mechanical relationship between the two is $\mu = \gamma h I/(2\pi)$, where h is Planck's constant and γ is the gyromagnetic ratio. For protons, $\gamma/2\pi = 42.6$ MHz/T.

In a single-volume element corresponding to a pixel in an MR image, there are many protons, each with an associated dipole magnetic moment, and the net magnetization, $M = M_x i + M_y j + M_z k$, of the volume element is the vector sum of the individual dipole moments, where i, j, and k are unit vectors along the x, y, and z axes, respectively. In the absence of a magnetic field, the spatial orientation of each dipole moment is random and $M = 0$.

This situation is changed by a static magnetic field, $B_0 = B_0 k$. This field induces magnetic moments to align them-
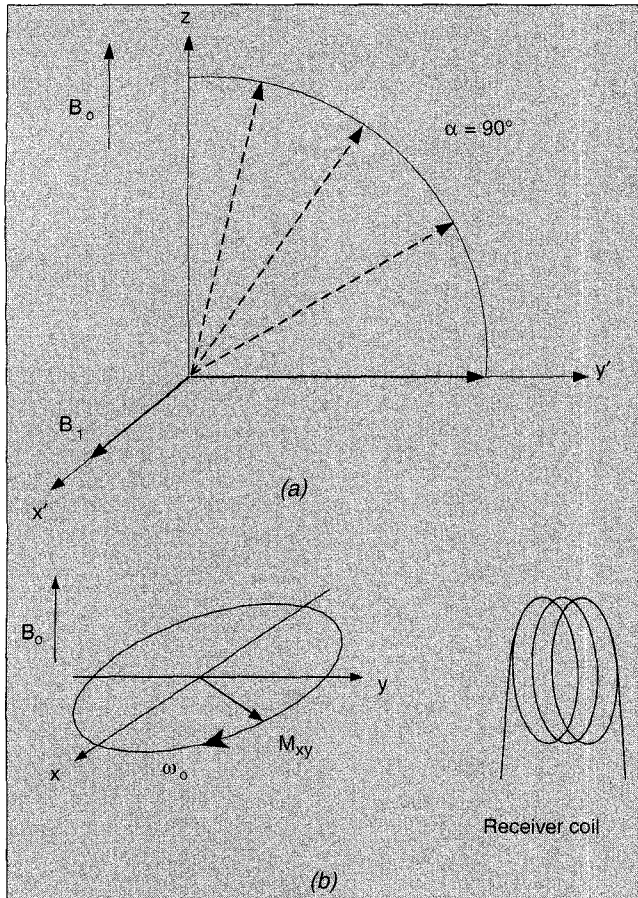
1. (a) Precession of net magnetization, **M**, around the applied radiofrequency (RF) field of field strength B_1, viewed in the rotating frame. The reference frame $x'y'z$ rotates around **B₀** at the Larmor frequency. (b) Nutation of M_{xy} in the laboratory frame at the Larmor frequency, ω_0, is proportional to the magnitude of the magnetic field, B_0. This oscillating magnetization induces an emf in the receiver coil.

selves in its direction, partially overcoming thermal randomization so that, in equilibrium, the net magnetization, **M** = M_0**k**, represents a small fraction (determined from the Boltzmann distribution) of $|\mu|$ times the total number of protons. Under typical imaging conditions (B_0 = 1.5 T—approximately 20,000 times the Earth's magnetic field strength, and temperature near 25°C), the magnitude of the equilibrium magnetization, M_0, roughly corresponds to 1 in 10^5 of the dipole moments in the volume being aligned with the field while the rest take on random orientations. While the fraction is small, the total number of contributing protons is very large at approximately 10^{15} dipoles in a 5 mm³ volume.

Equilibrium is not achieved instantaneously. Rather, from the time the static field is turned on, **M** grows from zero toward its equilibrium value M_0 along the z axis; that is,

$$M_z = M_0 \left(1 - \exp(-t / \text{T1}) \right), \tag{1}$$

where T1 is the *longitudinal relaxation time*. This equation expresses the dynamical behavior of the component of the net magnetization M_z along the longitudinal (z) axis.

The component of the net magnetization, M_{xy}, which lies in the *transverse plane* orthogonal to the longitudinal axis, undergoes completely different dynamics. M_{xy}, often referred to as the *transverse magnetization*, can be described by a complex quantity $M_{xy} = M_x + jM_y$, where $j = \sqrt{-1}$. This component *precesses* about **B₀**, i.e., $d\mathbf{M}(t)/dt = \gamma\mathbf{M} \times \mathbf{B_0}$. The precession frequency

$$\omega_0 = \gamma B_0 \tag{2}$$

is proportional to B_0 and is referred to as the *Larmor frequency* (Fig. 1b). This relation holds at the level of individual dipoles as well, so that $d\mu(t)/dt = \gamma\mu \times \mathbf{B_0}$.

Accompanying any rotating dipole magnetic moment is a radiated electromagnetic signal circularly polarized about the axis of precession; this is the signal detected in MRI. The usual receiver is a coil, resonant at ω_0, whose axis lies in the transverse plane—as M_{xy} precesses, it induces an electromotive force (emf) in the coil.

A final question remains: If **B₀** induces a collinear equilibrium magnetization **M**, how can we produce precessing magnetization orthogonal to **B₀**? The answer is to apply a second, time-varying magnetic field that lies in the plane transverse to **B₀**. Let this field be described by $\mathbf{B_1} = \cos(\omega_0 t)\mathbf{i} + \sin(\omega_0 t)\mathbf{j}$. This field rotates about the static field direction **k** at radian frequency ω_0. If we then place ourselves in a frame of reference $(x'y'z)$ that also rotates at radian frequency ω_0, this second field appears stationary. Moreover, any magnetization component orthogonal to **B₀** no longer appears to rotate about **B₀**. Instead, in this rotating frame, **M** appears to precess about the "stationary" field $\mathbf{B_1}$ alone with radian frequency γB_1. One can therefore choose the duration of $\mathbf{B_1}$, τ_{B1}, so that **M** is rotated into the transverse plane (Fig. 1b). The corresponding $\mathbf{B_1}$ waveform is called a 90° excitation pulse ($\gamma B_1 \tau_{B1}$ = $\pi/2$ radians).

The signal from M_{xy} will eventually decay. Part of this decay is the result of the drive to thermal equilibrium where **M** is brought parallel to **B₀**, as described earlier. However, this is generally a secondary contribution to the decay rate. Recall that the individual dipole moments contributing to **M** each precesses at a rate proportional to the magnetic field they experience. Since even a single-volume element contains a heterogeneous physical environment, the magnetic field varies slightly among its protons and the phase coherence present immediately after the 90° pulse is gradually lost as the dipole moments contributing to **M** precess at slightly different rates (Fig. 2a). Over time, the vector sum, **M**, decreases in magnitude since the individual dipole moments no longer add constructively. The associated decay is characterized by an exponential with time constant T2* (Fig. 2b).

Hahn [5] discovered that this loss of transverse magnetization due to dephasing can be recovered to some extent by inducing a *spin echo* (Fig. 2). Specifically, let the dipole moments evolve for a time, τ, after excitation. At this time, apply another $\mathbf{B_1}$ field along y' (see Fig. 1b) to rotate the dipole moments 180° around $\mathbf{B_1}$. This occurs in a time that is

very short compared to τ. This pulse effectively negates the phase of the individual dipole moments that have developed relative to the axis of rotation of the refocusing pulse. Assuming the precession frequencies of the individual dipole moments remain unchanged then at a time, τ, after the spin-echo or 180° pulse, the original contributions of the individual dipoles refocus (Fig. 2a). Hence, at a time TE = 2τ after the excitation, the net magnetization is the same as it was just after excitation.

In practice, some signal is lost because the precession frequencies are not time-independent—they fluctuate randomly. This produces a phase dispersion among the moments that cannot be reversed with a refocusing pulse. If one applies a periodically spaced train of such 180° pulses following a single excitation, one observes that the envelope defined by $\left|M_{xy}\right|$ at each echo time steadily decays (Fig. 2b). This irreversible signal loss is often modeled by an exponential decay with time constant T2, the *transverse relaxation time*:

$$\left|M_{xy}\right| = M_0 \exp(-t/T2). \tag{3}$$

Before the experiment can be repeated with another excitation pulse, sufficient time must elapse to re-establish equilibrium magnetization along $\mathbf{k}$. As indicated in Eq. (1), a sequence repetition time, TR, of several T1s is necessary for full recovery of equilibrium magnetization, M_0, along M_z between excitations.

All of the dynamics of net magnetization described so far can be encapsulated in a single equation known as the *Bloch equation* [1]:

$$\frac{d\mathbf{M}(t)}{dt} = \mathbf{M}(t) \times \gamma\mathbf{B}(t) - \left(M_x(t)\mathbf{i} + M_y(t)\mathbf{j}\right)/T2 \tag{4}$$
$$-\left(M_z(t) - M_0\right)\mathbf{k}/T1,$$

where $\mathbf{B}$ is the total magnetic field. This equation forms the basis of MR excitation sequences and subsequent signal acquisition and processing.

Imaging, Contrast, and Noise

The signal detected from an anatomical region is the sum of the signals from dipoles all over the region. In order to form an image, the dipoles must somehow be spatially resolved. This is usually a two-step process: (i) exciting the magnetization into the transverse plane over a spatially restricted region, and (ii) encoding spatial location of the signal during data acquisition. For medical applications, the image must reflect clinically relevant anatomy and physiology. One way of achieving this is by manipulating image contrast with appropriate data-acquisition parameters. Ultimately, image quality is constrained by noise, which enters MRI in an interesting way. The basic principles of image formation, contrast manipulation, and signal-to-noise ratio (SNR) are introduced in the following sections. In each section, the role of signal processing is highlighted.
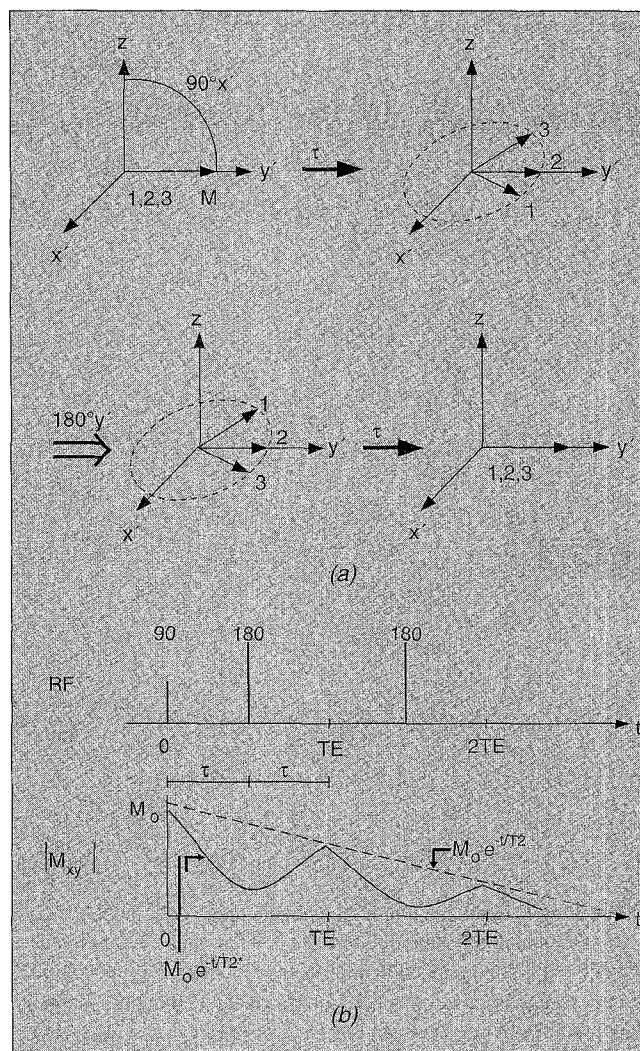
2. (a) Spin echo generation, demonstrated with three representative dipoles, μ_1, μ_2, and μ_3. Each dipole is in a different magnetic field so that each has a different Larmor frequency; that of μ_1 is fastest, while that of μ_3 is slowest. The dipoles are viewed in the rotating frame $(x'y'z)$ in which μ_2 appears stationary. After the initial excitation, the dipoles precess for time τ. μ_3 lags behind μ_2 and μ_1 is ahead. At this time, a "refocusing" pulse is applied to flip the vectors 180° about the y' axis. As a result, μ_3 is placed ahead of μ_2 and μ_1 behind. After further time τ, μ_3 catches up to μ_2 and μ_1 loses its lead, so that all three are again aligned. (b) Decay of transverse magnetization, $\left|M_{xy}\right|$, in the presence of a train of refocusing pulses. The envelope of the decay at the echo times $n \times TE$ is often described by an exponential with time constant T2, while decay after each echo is characterized by the time constant T2*.

Spatially Selective Excitation

The usual goal in spatially selective excitation is to tip magnetization in a thin spatial slice or section, say of thickness Δz along the z axis, into the transverse plane. Conceptually, this is accomplished by first causing the Larmor frequency to vary linearly in one spatial dimension, $\mathbf{B}(z) = (G_z(z - z_0) + B_0)\mathbf{k}$, and then, while holding the field constant, applying a

radiofrequency (RF) excitation pulse crafted to contain significant energy only over a limited range of temporal frequencies (BW) corresponding to the Larmor frequencies in the slice. To a first approximation, the amplitude of the component at each frequency in the excitation signal determines the flip angle of the protons resonating at that frequency. As a result, if the temporal Fourier transform of the pulse has a rectangular distribution about ω_0, a rectangular distribution of spins around z_0 is tipped away from the z axis over a spatial extent $\Delta z = 2\pi BW/\gamma G_z$. For small tip angles (generally, $\leq \pi/2$), we can solve the Bloch equations explicitly to get the spatial distribution of M_{xy} following an RF pulse, $B_1(t)$, in the presence of a magnetic field gradient of amplitude G_z:

$$\left| M_{xy}(z) \right| = \gamma M_0 \mathcal{F}\left\{ B_1(t) \right\}_{f=\gamma G_z z/2\pi}, \tag{5}$$

where $\mathcal{F}\{\}$ is the one-dimensional (1D) Fourier transform with frequency f. Assume that all the magnetization initially lies along the z axis. Under these conditions, a rectangular slice profile is achieved if $B_1(t) = \text{sinc}(BWt)(\cos(\omega_0 t)\mathbf{i} + \sin(\omega_0 t)\mathbf{j})$.

Signal processing methods have been applied to improve the accuracy and to extend the applications of selective excitation. For 1D excitation, the sharpness of the edge and the degree of suppression in the stopband have been improved by taking into account the nonlinear nature of the Bloch equation [6, 7]. More recently, the Shinnar-LeRoux algorithm has been developed to transform 1D pulse design into a finite-impulse-response digital filter design problem, where many standard digital signal processing tools can be applied [8]. Selective excitation has also been extended to multiple spatial dimensions through linear systems theory under the small-tip Fourier approximation [9]. The two-dimensional (2D) case is the dual of spatial encoding, which is described in the following section.

Image Formation Through Spatial Frequency Encoding

The Imaging Equation
Once one has isolated a volume of interest using selective excitation, the volume can be imaged by manipulating the precession frequency (determined by the Larmor relation (Eq. 2)), and hence the phase of M_{xy} [4]. For example, introduce a linear magnetic field gradient, G_x, in the x direction so that $\mathbf{B}_0(t) = (G_x x + B_0)\mathbf{k}$; each dipole now contributes a signal at a frequency proportional to its x-axis coordinate.

Table 1. NMR parameters for tissues in the head at 1.5 T		
Tissue	T1 (ms)	T2 (ms)
Gray Matter	1000	106
White Matter	650	69
Fat	260	60
Cerebrospinal Fluid	4000	2300

In principle, by performing a Fourier transform on the received signal, one can determine M_{xy} as a function of x. An equivalent point of view follows from observing that each dipole contributes a signal with a phase that depends linearly on its x-axis coordinate and time. Thus, the signal as a whole samples the spatial Fourier transform of the image along the k_x spatial frequency axis, with the sampled location moving along this axis linearly with time.

A more general viewpoint can be developed mathematically from the Bloch equation. For simplicity, the problem is limited to producing a spatial map in two dimensions, x and y. In practical situations, this is achieved using spatially selective excitation (described earlier) where only protons in a thin slice at $z = z_0$ are tipped into the transverse plane so that $M_{xy}(x,y) = M_{xy}(x,y,z_0)$ [3]. Let the magnetic field after excitation be $\mathbf{B} = (B_0 + G_x x + G_y y)\mathbf{k}$; assume $\left| M_{xy} \right|$ is relatively constant during data acquisition (i.e. acquisition duration << T1,T2,T2*); and let the time at the center of the acquisition be t_{acq}. During acquisition,

$$M_{xy}(x,y,t) = \left| M_{xy}(x,y,t_{acq}) \right| \exp(-j\omega_0 t) \times \tag{6}$$
$$\exp\left(-j\gamma \int_0^t \left(G_x(t')x + G_y(t')y \right) dt' \right).$$

The signal received, $S(t)$, is the integral of this signal over the xy plane. Letting $k_x(t) = \gamma \int_0^t G_x(t') dt'$ and $k_y(t) = \gamma \int_0^t G_y(t') dt'$,

$$S(t) = \exp(-j\omega_0 t) \int_x \int_y \left| M_{xy}(x,y,t_{acq}) \right| \times \tag{7}$$
$$\exp(-j)(k_x(t)x + k_y(t)y) dx dy.$$

If this signal is demodulated by ω_0 then the resulting baseband signal, $S_e(k_x(t), k_y(t))$, is the 2D spatial Fourier transform of $\left| M_{xy}(x,y,t_{acq}) \right|$ [10] at spatial frequency coordinates $k_x(t)$ and $k_y(t)$. One chooses $G_x(t)$ and $G_y(t)$ so that, over the full data acquisition, the 2D frequency domain is adequately sampled and the desired image can be reconstructed as the inverse Fourier transform of the acquired data.

Image Characteristics—Sampling Issues
In general, the (k_x, k_y) frequency domain, referred to as k space, cannot be sampled completely after a single excitation. This is because of a variety of physical limitations (finite relaxation time of the dipoles and SNR limitations) and technical limitations (slew rate limits on $G_x(t)$ and $G_y(t)$). Thus, k space is sampled in a sequence of n excitation-acquisition cycles with repetition time TR.

The most popular method of sampling k space is referred to as 2D Fourier transform (2DFT) or spin-warp imaging [11]. During each acquisition, this method samples the signal along a line in k space corresponding to k_y = some constant. The subsequent $n - 1$ acquisitions interrogate all the relevant k_x frequencies at incremental values of k_y until k space is sampled sufficiently in a grid centered at the origin. The

imaging time is therefore $n \times$ TR. The gradient and data acquisition pattern as well as the resulting trajectory in (k_x, k_y) space are illustrated in Figs. 3a and 3b.

The effect of the k-space sampling pattern on the image is described by Fourier transform theory. From the Nyquist sampling theorem, the spacing between data points in k_y determines the period with which the image is repeated (aliasing). Thus, the sampling interval Δ_{k_y} determines field of view in y as $FOV_y = 1/\Delta_{k_y} = 2\pi/\gamma\Delta_{G_y}\tau_y$, where Δ_{G_y} and τ_y are defined in Fig. 3. To avoid aliasing artifacts, FOV_y should be greater than the extent of the object in the y dimension. Similarly, $FOV_x = 1/\Delta_{k_x} = 2\pi/\gamma\, G_{xr}\tau_{AD}$ (see Fig. 3). Note that aliasing can be avoided in x for the 2DFT acquisition by using a temporal frequency filter on the received signal.

The resolution of the image depends on the range of spatial frequencies sampled in the two dimensions. Specifically, one can consider the k-space coverage as multiplying the Fourier transform of the object by a 2D box or rect function of dimensions $W_{kx} \times W_{ky}$. The resulting image after the Fourier transform will be the spatial distribution of the signal in the object convolved by the blurring function $sinc(W_{kx}x)sinc(W_{ky}y)$ [12]. Thus, the resolution in x is $\delta_x = 1/W_{kx} = 2\pi/\gamma\, G_{xr}\tau_x$, and in y it is $\delta_y = 1/W_{ky} = 2\pi/2\gamma\, G_{yp}\tau_y$.

Field of view and resolution are related by the number of data points acquired in each dimension. For example, $FOV_x = \delta_x/N_{kx}$, where N_{kx} is the number of points acquired in k_x. In 2DFT acquisitions, one can always increase FOV_x by reducing the sampling interval τ_{AD}. However, lines in k_y are acquired at intervals of TR and, thus, there is a direct trade-off between field of view, resolution, and imaging time in this dimension. Typically, one acquires 256×256 data points in k space distributed so that the field of view is about 24 cm (for the head). Thus, in-plane resolution is roughly 1×1 mm. Slice thickness is typically about 5 mm yielding a voxel volume of 5 mm^3. If TR $= 1$ s, the total imaging time is 4 min, 16 s for a 2DFT acquisition. Increasing field of view or resolution will result in a parallel increase in imaging time.

Rapid Imaging

For early sequences, data acquisition for a single image required minutes or tens of minutes. A great deal of research has targeted more rapid imaging methods. Newer methods of scanning k space reduce imaging times by acquiring multiple lines in k_y after a single excitation [13] or after an interval of contrast preparation [14]. Alternatively, one can scan more of k space after each excitation following different trajectories using time-varying gradients [15].

Design of these rapid acquisitions must address several issues. One must consider how the MR signal behavior changes as k space is scanned. As acquisition duration after a single excitation becomes longer, the assumption that M_{xy} is constant over the acquisition interval loses validity. Signal variations associated with T2 or T2* decay or accumulation of phase due to error in ω_0 modulate the data as a function of k-space position, introducing distortions into the image referred to as artifacts (see the "Image Artifacts" section). All rapid imaging techniques must overcome this problem. In
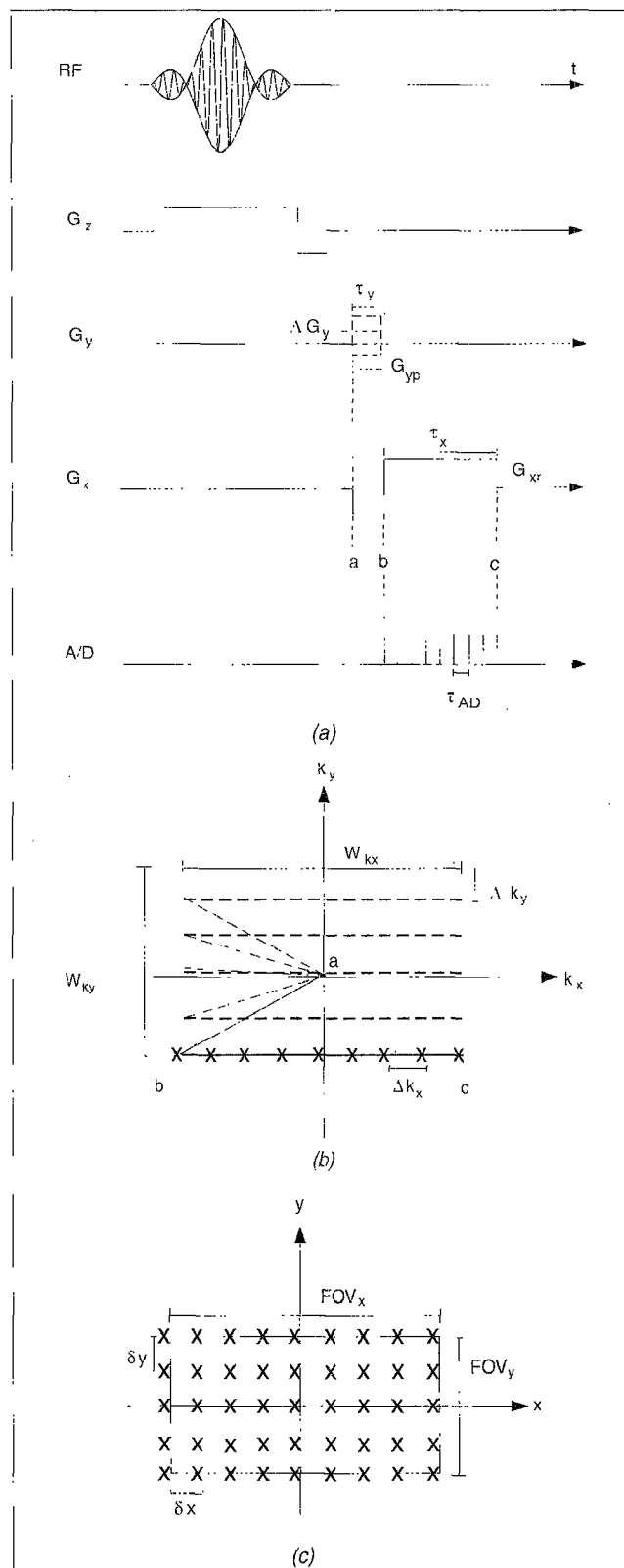
3. (a) Sequence for 2DFT k-space scanning. After slice selection, gradients move to the position in (kₓ,kᵧ) where acquisition is to begin. The data acquisition (A/D) is then turned on and a line in kₓ is scanned by setting Gₓ to a constant value and Gᵧ to zero. Subsequent acquisitions alter the kᵧ position at which acquisition starts. (b) Scanning of k space corresponding to the 2DFT sequence in (a). (c) Coverage of the image associated with the k-space trajectory in (b).

addition, methods using time-varying trajectories must take into account gradient amplifier constraints—the maximum linear velocity in k space is limited by maximum current amplitude while the ability to turn corners in k space is limited by the maximum slew rate. Finally, time-varying gradients often yield k-space data that do not lie on Cartesian coordinates. While 2DFT acquisitions can be reconstructed directly using a 2D FFT algorithm, non-Cartesian data are interpolated and re-sampled onto a Cartesian grid prior to this operation. In this situation, nonuniform sampling density in k space must also be accounted for [16, 17].

In current systems, complete image acquisitions can take less than 100 ms while partial image updating can be performed even more rapidly. These improvements in turn drive a demand for more rapid digital signal processing software and hardware as well as improved display and control capabilities.

Contrast in MR Images

Protons in environments corresponding to different materials have different longitudinal and transverse relaxation times, T1 and T2. For instance, the T1s and T2s of materials in the head at a field strength of 1.5 T are listed in Table 1 [18]. The differences between these parameters are used to produce contrast between these materials in an MR image. Moreover, by timing the acquisitions correctly, one can ensure that $\left|M_{xy}(x,y,t_{acq})\right|$ quantitatively reflects these parameters. For instance, by acquiring a signal at a relatively late spin echo
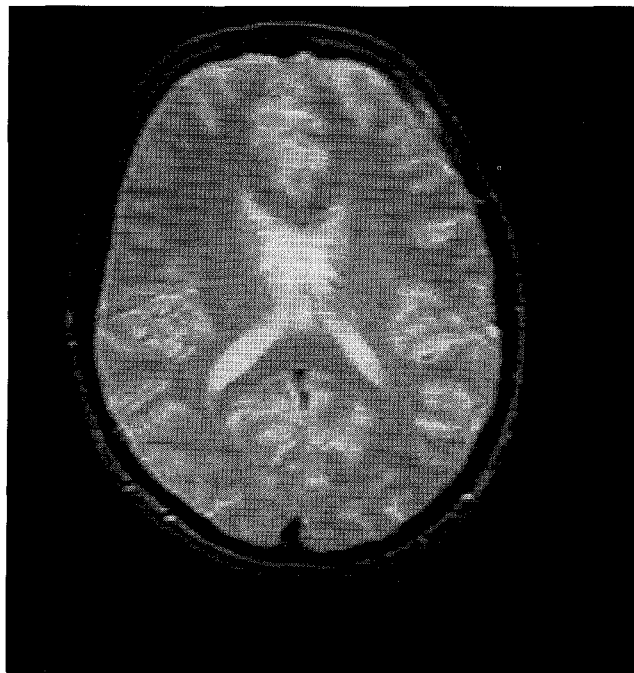
4. T2-weighted image of an axial slice through the head. This image was acquired at an echo time of TE = 70 ms. Acquisition was repeated every TR =2000 ms until 128 lines in k_y were acquired. Field strength = 1.5 T.

time, TE, and waiting a long time between acquisitions (TR >> T1 for all materials in the volume of interest), the signal is strongly weighted by T2. From Eq. (3) and Fig. 2, the magnitude of the acquired signal at different positions in the image is

$$\left|M_{xy}(x,y,t_{acq}=TE)\right| = \tag{8}$$
$$M_0(x,y)\exp(-TE / T2(x,y)).$$

This is illustrated in a T2-weighted image of the head with TE = 70 ms (Fig. 4). In accordance with the relative T2s, the signal gets progressively brighter as one shifts from regions of fat (at edge) to white matter to gray matter to cerebrospinal fluid.

To get T1 weighting in an image, one reduces TR so that magnetization does not recover fully between excitations. If the signal is acquired immediately after the 90° excitation, it depends primarily on the T1 of the material in the corresponding volume. From Eq. (1), the signal at each position in the image is

$$\left|M_{xy}(x,y,t_{acq}=0)\right| = \tag{9}$$
$$M_0(x,y)\left[1-\exp(-TR / T1(x,y))\right].$$

This is called the *saturation recovery sequence.*

More generally, one can choose sequence parameters to take advantage of a mixture of T1, T2, and T2* differences between soft tissues as well as slight shifts in frequency between protons in different environments (notably water versus fat). One can also differentially encode flowing versus stationary spins or one can introduce contrast agents orally or intravenously to alter the signal response in the neighborhood of these agents.

The flexibility of MR contrast represents an exciting opportunity for the depiction of anatomical and functional information of use in many clinical applications. With this flexibility, however, comes the challenge of optimizing the acquisition parameters for the task at hand [19]. To date, limited quantitative characterization of NMR tissue parameters and the variability in these characterizations [20] have restricted the use of numerical optimization for the selection of imaging parameters such as tip angle, TR, and TE.

Efforts in this direction are progressing, however, for targeted applications. Flow-independent angiography isolates the arterial blood signal from surrounding tissues in the limbs by exploiting T1, T2, and frequency differences among the tissues in the volume [21]. This method has been developed to map vascular anatomy in patients with peripheral vascular disease [22, 23]. Furthermore, quantitative characterization of a significant relationship between the T2 of blood and its oxygen content is leading to noninvasive, *in vivo* measures of vascular oxygen content with MRI [24, 25]. These are just a few examples of the potential to be realized from the rich amount of information in the MR signal.
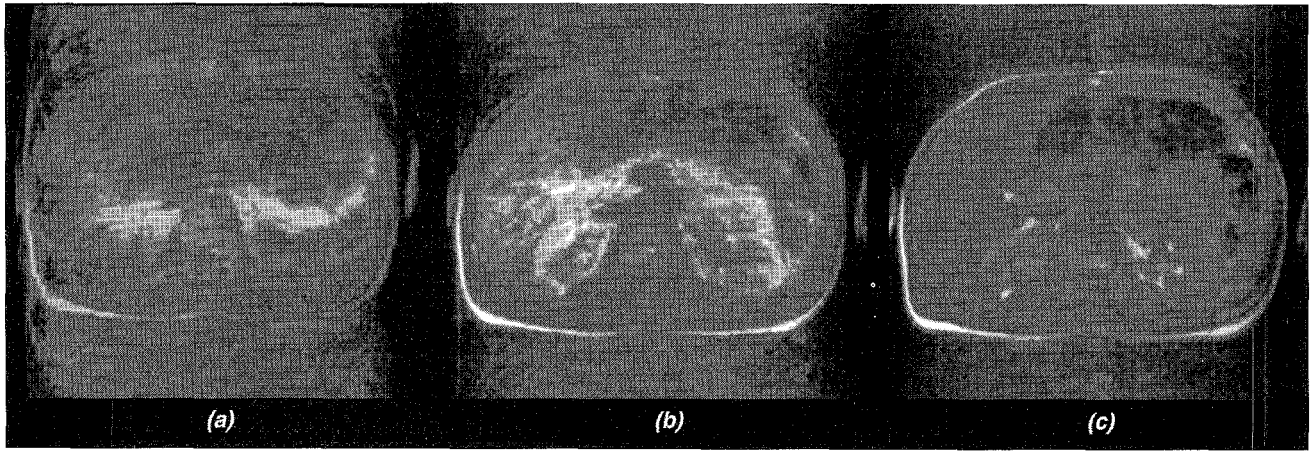
5. *Images of an axial slice through the abdomen of a healthy volunteer. Imaging parameters are as follows: $TR = 0.7$ s; $TE = 48$ ms; $FOV_x = FOV_y = 36$ cm; $\delta_y = 2\delta_x = 3$ mm; slice thickness = 10 mm; field strength = 1.5 T; image acquisition time is 90 s for each of (a) and (b) and 13 s for (c). For images (a) and (b), the subject is breathing regularly with a respiratory period of about 5 s. Image (c) is a breath-held acquisition. Image (a) is acquired by incrementing k_y systematically from $-W_{ky}/2$ to $W_{ky}/2$; (b) is acquired by ordering acquisition at different k_y based on concurrent measures of chest expansion so that displacement versus k_y is given by Fig. 6. (c) Breath-held acquisition using a fast spin-echo sequence where 8 lines in the k_y dimension are acquired in each TR interval.*

Signal and Noise Considerations

As noted earlier, the signal received from a given voxel is the voltage induced by the precessing magnetization vector **M**. The amplitude of this vector depends on the relative fraction of dipole moments aligned with the static field before the excitation pulse and is proportional to B_0. The signal is also proportional to the time rate of change of the signal from **M**, i.e., to ω_0 and thus B_0 again. The voltage signal thus shows a B_0^2 dependency. A signal associated with a particular voxel will depend on the total number of protons in the voxel and is thus proportional to the voxel volume.

The fundamental source of random noise in the image is the thermal emf generated in the receiver coil by the body itself. From the Nyquist reciprocity theorem [26], this noise can be viewed equivalently as Johnson noise from the resistive impedance of the receiver coil loaded by the body. The Johnson noise can be characterized as a white, Gaussian random process with zero mean added onto the signal, whose variance is proportional to the resistive impedance. This resistance is proportional to ω_0^2 and hence B_0^2. It is also roughly proportional to the square of the sample volume seen by the coil, referred to as the *noise volume*. Thus, receiving with coils that are only sensitive to the volume of interest reduces noise. Beyond that, increasing coil sensitivity will not affect the ratio of the signal to the standard deviation in the noise (SNR) as it has the same effect on the signal and the noise term. Finally, since noise averages incoherently while signal averages coherently, SNR will improve as the square root of the total data acquisition time, T_{acq}. Thus [27],

$$\text{SNR} \propto B_0 \times \frac{\text{voxel volume}}{\text{noise volume}} \sqrt{T_{acq}} \, . \tag{10}$$

This equation describes the tradeoffs between field strength, resolution, acquisition time, and SNR. Clearly, the development of imaging sequences that are faster and/or produce images at higher resolution incur an SNR penalty. Efforts to reduce system cost by reducing magnet field strength incur a similar penalty. Thus, a great deal of effort has been invested in methods to reduce noise.

When one contemplates post-processing techniques for noise reduction, however, the nature of the data acquisition must be borne in mind. For example, a very simple method to reduce noise in an image is to perform spatial averaging over groups of pixels. Averaging two adjacent pixels will improve SNR by a factor of $\sqrt{2}$ when the noise in the individual pixels is independent (as it should be for carefully chosen acquisition parameters). The process of averaging adjacent pixels essentially reduces the resolution and, hence, the maximum spatial frequency in one dimension by a factor of 2. Thus, one effectively throws away half the acquired data. From Eq. (10) the process of pixel averaging increases voxel volume by a factor of 2 and reduces effective T_{acq} by a factor of 2, yielding the expected $\sqrt{2}$ improvement in SNR. However, if one had known at data acquisition time that half the resolution was sufficient, one could have spent twice the time acquiring data at the lower spatial frequencies rather than gathering data that would later be discarded. The result would be an image with the same resolution as the spatially averaged image but with $\sqrt{2}$ greater SNR than the image produced by averaging adjacent voxels. The critical lesson here is that one should acquire data for the image resolution necessary for the application, but acquisition of excessive resolution is extremely costly in terms of SNR. SNR loss due to excessive resolution at data acquisition cannot be economically recovered by subsequent spatial averaging [28].

Image Artifacts—Characterization and Correction

MR images often contain distortions and spurious features that are collectively described as *artifacts*. In many cases, artifacts can be traced to sampling issues in k space. Some simple examples are: (i) inadequate sampling in one dimension (Δk_y too large), leading to signal wrap-around or aliasing; (ii) abrupt truncation of the sampling at high spatial frequencies where the object has energy beyond the truncation point, leading to Gibbs ringing at edges in the image; and (iii) spurious signal at isolated time points during data acquisition, which introduces excessive energy at specific spatial frequencies and leads to striping across the image. These and other artifacts are well described in a comprehensive review on the subject [29].

Efforts to characterize and reduce these artifacts inevitably involve linear systems theory applied in the spatial-frequency domain. Below, the specific case of imaging an axial slice through the abdomen of a healthy volunteer is considered as an illustrative case. The abdomen moves during the acquisition as the subject breathes, and artifacts, in this situation "ghosts," appear if motion is ignored in the imaging strategy (Fig. 5a).

A very simple model of the motion in this volume, particularly the motion of the chest wall, is a sinusoidal bulk displacement in the anterior-posterior direction (the y direction in this discussion) of amplitude A and period $T_B \approx 5$ s. Consider the case of spin-warp imaging, where k space is filled in a grid pattern (described earlier). Conceptually, the n_{k_y} horizontal line in the grid is acquired by first exciting the slice and then moving to $k_y = -W_{ky} / 2 + n_{k_y} \times \Delta k_y$. Data for all k_x values corresponding to that k_y are acquired shortly thereafter. If, however, the object represented by the magnetization distribution $M_{xy}(x,y)$ has shifted in y by an amount $\varepsilon_y \left[n_{k_y} \right]$ at the time the spatial frequency k_y is encoded, $M_{xy}(x,y)$ must be replaced by $M_{xy}\left(x, y - \varepsilon_y\left[n_{k_y}\right]\right)$ in Eq. (7) for that acquisition. By a change of variables, one can see that this introduces an additional phase term $k_y \varepsilon_y\left[n_{k_y}\right]$ for that k-space line. Every TR, the index n_y is incremented and a new phase error is introduced depending on the position shift $\varepsilon_y\left[n_{k_y}\right]$. In Fig. 5, TR = 700 ms so that an entire image acquisition consisting of 128 k_y encodes requires 90 s corresponding to about 18 breathing cycles. Based on the model, $\varepsilon_y\left[n_{k_y}\right] = A \sin\left(2\pi n_{k_y} \text{TR} / T_B\right)$ across the k_y dimension. Thus, 18 periods of phase variation are introduced across k_y. Mathematically, the motion-corrupted k-space representation of the slice, $\hat{S}\left(k_x, k_y\right)$, is given by

$$\hat{S}\left(k_x, k_y\right) = S\left(k_x, k_y\right) \times \exp\left(-jA k_y \sin\left(2\pi n_{k_y} \text{TR} / T_B\right)\right) \qquad (11)$$

where S is the true representation of the slice [30].

To consider the effect on the resultant image, one takes the Fourier transform. The result is the correct image convolved in the y-dimension by a series of narrow point-spread functions spaced by $(\text{TR}/T_B) \times \text{FOV}_y$ [30]. The result is a series of image ghosts of various intensities at these shifted positions. The ghosts can produce severe image degradation (Fig. 5a).

This kind of artifact can be reduced significantly by using *a priori* information about the object's position as each line in k space is scanned. For instance, one can measure the chest expansion during the acquisition with a transducer. The strategy is to scan the lines out-of-order so that the displacement will vary monotonically with k_y [31] (Fig. 6). Assuming a linear relation between the y displacement and k_y, the k-space representation of the slice is now

$$\hat{S}\left(k_x, k_y\right) = S\left(k_x, k_y\right) \times \exp\left(-j2A\left(k_y\right)^2 / W_{ky}\right), \qquad (12)$$

where W_{ky} is defined in Fig. 3. The resulting image is the original object convolved in y by a single blurring point-spread function. This method has been used in Fig. 5b to improve significantly the depiction of abdominal anatomy in the presence of respiratory motion.

The general strategy here is to guide the k-space filling pattern with prior knowledge of temporal changes in the MR signal from the volume of interest so that modulation of the true k-space representation varies as gradually and smoothly as possible with k_x and k_y. The result is a point-spread function with a single narrow peak. This strategy has been successfully applied in many MR imaging situations where image contrast varies over the duration of k-space filling.

k-space re-ordering is just one example of a broad range of motion-correction schemes developed in MRI. Some other approaches include data correction following acquisition,
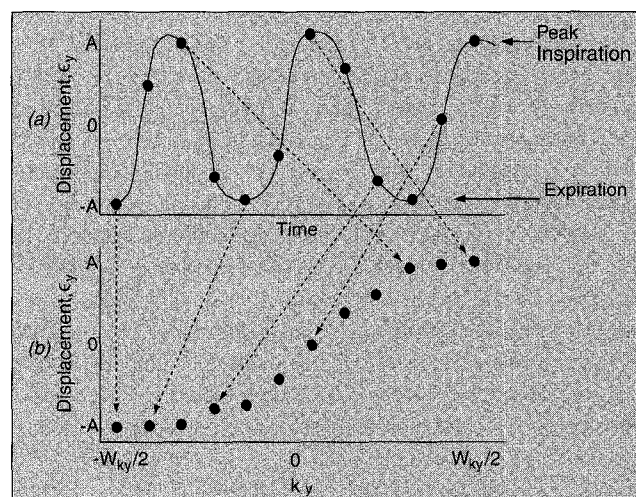
6. *k-space filling strategy to reduce motion artifacts. (a) Displacements of the chest are measured at the time of each acquisition of a line in k space. In (b), instead of the standard strategy of incrementing k_y from $-W_{ky}/2$ to $W_{ky}/2$ over the duration of the image scan, measures of displacement are used to select the appropriate k_y value at that instant so that displacement varies monotonically with k_y.*

synchronized acquisitions, and rapid acquisitions with motion suspended. Examples of these are briefly outlined below.

When bulk in-plane displacement is a reasonable model of the motion, concurrent measures of this displacement can be used to correct the image [32, 33]. For instance, knowing the position shift in y for data at a given k_y in the previous example, one can correct the data by multiplying the k-space line by the inverse of the corrupting phase term in Eq. (11). Unfortunately, this approach is restricted to very simple motions.

Another approach involves synchronizing data acquisition with motion so that all measurements are made when the volume is in the same position. However, this often leads to excessively long imaging times. One strategy to reduce imaging time is to again record the volume displacement each time a line in k space is scanned; after acquisition of a complete data set, lines corresponding to displacements furthest from the mean position are re-acquired. The image is thus progressively refined until either a fixed time has elapsed or until some criterion for image quality is reached [34].

The previous methods are limited to cases where motion is approximately periodic. Wherever possible, a more robust solution is to image the volume in a time that is short compared to the motion. The specific challenge of respiratory motion effects on single-slice acquisition now can be overcome by suspending the motion with a breath-hold and rapidly acquiring the image. In Fig. 5c, 8 lines in k space are acquired per TR, one per echo in a spin-echo train (Fig. 2b). Imaging time is reduced by a factor of 8 so that the entire image is acquired in 13 s, a comfortable breath-holding interval. However, the extended acquisition period each TR can introduce new artifacts as the signal is modulated as a function of k_y by T2 signal decay. Analogous to the motion-correction strategy in Fig. 6, artifacts are minimized by ordering acquisitions so that signal change over k_y is smooth and slowly varying [35]. The T2-weighted contrast in the image is determined by the TE used for signal acquisitions at the lowest spatial frequencies (where most signal energy resides). In Fig. 5c, low spatial frequencies are acquired at TE = 48 ms so that contrast is similar to Fig. 5b.

Rapid imaging is not, alone, the complete solution to motion artifacts. Cardiac motion, for example, is too fast to be "frozen" by current rapid imaging methods; observe, in Fig. 5c, the ghosting that results from cardiac pulsatility in the aorta. Furthermore, continuing pressures for higher resolution (with the associated SNR penalty) and for imaging extensive three-dimensional (3D) volumes lead to longer imaging times. Suppression of motion artifacts in these situations requires a creative combination of strategies.

Image Analysis

The nature of the data produced with MRI is, in many ways, well-suited to subsequent image analysis. Specifically, (i) many different organs can be distinguished with the flexible soft tissue contrast; (ii) resolution can be tailored to specific applications and noise is generally well behaved; (iii) a signal can be resolved in the three spatial dimensions to submillimeter levels; (iv) one can resolve temporal signal changes at the subsecond level; and, finally, (v) one can obtain multiple measurements of the same volume element with different contrast characteristics. The vast volume of data alone often demands computer image analysis for interpretation and display.

Areas of research in image analysis include methods for image segmentation [36-39] and registration [38, 40-43]. Image segmentation facilitates (i) volume estimation for characterizing disease (ejection fraction in the heart, tumor volumes), (ii) isolation of a tissue of interest from a 3D data set, notably for the display of vascular anatomy, and (iii) multiple image registration through the identification of common landmarks in the images. Registration facilitates (i) temporal signal analysis of a specified volume within the same study, (ii) comparative studies of the same patient over multiple studies perhaps with data of different contrast weightings or even data from different imaging modalities, and (iii) comparative studies of anatomy across multiple individuals.

The task of image analysis is simplified greatly when attention is paid to the nature of the basis images. As noted previously, image sequence parameters can be selected to maximize contrast between tissues, facilitating segmentation. Acquisition can be synchronized to motion or priority can be given to imaging speed to reduce the demands on registration algorithms. Similarly, registration of multiple images with different contrasts is aided by acquiring lines of k space from the different images in a time-interleaved manner. For segmentation, image resolution should be selected to minimize the difficulties associated with partial voluming, where multiple tissues are present in the same voxel, based on the sizes of the structures of interest. Finally, the additive, Gaussian nature of the noise can be exploited to optimize classification strategies in segmentation. As a caveat, the noise takes on a Rician distribution in magnitude images most often used for segmentation as a result of the magnitude operation.

Summary

Signal processing tools are fundamental to MRI, from the design of acquisition strategies through to the analysis of the resulting images. Linear systems theory and digital filter design are used to spatially localize the signal of interest through selective excitation. Data acquisition occurs in the spatial-frequency (k-space) domain where sampling theory determines resolution and field of view. Strategies for reducing image artifacts are often best developed in this domain. Image reconstruction involves fast multidimensional Fourier transforms, often preceded by data interpolation, re-sampling, and apodization. The resulting large digital data sets lend themselves to computer image analysis. Considerations for image analysis either performed by the computer or an expert observer begin with appropriate selection of acquisition parameters, and there is a great deal of flexibility in

trading off SNR and resolution and maximizing contrast between tissues of interest at this stage. As the quality of the data continues to improve with better hardware, imaging sequences, and analysis tools, new clinical applications are being developed for this very flexible, noninvasive modality. With these applications come greater challenges for the underlying signal processing.

Acknowledgments

G.A. Wright is an Assistant Professor in the Sunnybrook Health Science Centre's Dept. of Medical Biophysics at the University of Toronto, Toronto, Ontario.

1. F. Bloch, "Nuclear induction," *Physical Review*, vol. 70, pp. 460-473, 1946.

2. E. Purcell, H. Torrey, and R. Pound, "Resonance Absorption by Nuclear Magnetic Moments in a Solid," *Physical Review*, vol. 69, pp. 37-38, 1946.

3. A. Garroway, P. Grannell, and P. Mansfield, "Image Formation in NMR by a Selective Irradiative Pulse," *J. Phys. C: Solid State Phys.*, vol. 7, pp. L457-L462, 1974.

4. P. Lauterbur, "Image Formation by Induced Local Interactions: Examples Employing Nuclear Magnetic Resonance," *Nature*, vol. 242, pp. 190-191, 1973.

5. E. Hahn, "Spin echoes," *Physical Review*, vol. 80, pp. 580-594, 1950.

6. S. Conolly, D. Nishimura, and A. Macovski, "Optimal Control Solution to the Magnetic Resonance Selective Excitation Problem," *IEEE Transactions on Medical Imaging*, vol. MI-5, no. 2, pp. 106-115, 1986.

7. J. Murdoch, A. Lent, and M. Kritzer, "Computer-Optimized Narrowband Pulses for Multislice Imaging," *Journal of Magnetic Resonance*, vol. 74, pp. 226-263, 1987.

8. J.M. Pauly, P. Le Roux, D. Nishimura, and A. Macovski, "Parameter Relations For the Shinnar-Le Roux RF Pulse Design Algorithm," *IEEE Transactions on Medical Imaging*, pp. 53-65, March 1991.

9. J. Pauly, D. Nishimura, and A. Macovski, "A k-space Analysis of Small-Tip-Angle Excitation," *Journal of Magnetic Resonance*, vol. 81, pp. 43-56, 1989.

10. D.B. Tweig, "The k-trajectory Formulation of the NMR Imaging Process with Applications in Analysis and Synthesis of Imaging Methods," *Medical Physics*, vol. 10, no. 5, p. 610, 1983.

11. A. Kumar, D. Welti, and R.R. Ernst, "NMR Fourier Zeugmatography," *Journal of Magnetic Resonance*, vol. 18, pp. 69-83, 1975.

12. R. Bracewell, *The Fourier Transform and its Applications*. San Francisco: McGraw-Hill Book Company, 1978.

13. J. Hennig, A. Nauerth, and H. Friedburg, "RARE Imaging: a Fast Imaging Method for Clinical MR," *Magnetic Resonance in Medicine*, vol. 3, pp. 823-833, 1986.

14. A. Haase, "Snapshot FLASH MRI. Applications to T1, T2, and Chemical-Shift Imaging," *Magnetic Resonance in Medicine*, vol. 13, no. 1, 1990.

15. P. Mansfield, "Multi-Planar Image Formation Using NMR Spin Echoes," *Journal of Physics C*, vol. 10, pp. L55-L58, 1977.

16. J.I. Jackson, C.H. Meyer, D. G. Nishimura, and A. Macovski, "Selection of a Convolution Function for Fourier Inversion Using Gridding," *IEEE Transactions on Medical Imaging*, vol. 10, pp. 473-478, 1991.

17. C. Meyer, B. Hu, D. Nishimura, and A. Macovski, "Fast Spiral Coronary Artery Imaging," *Magnetic Resonance in Medicine, vol. 28, pp. 202-213, 1992.*

18. P. Bottomley, T. Foster, R. Argersinger, and L. Pfeifer, "A Review of Normal Tissue Hydrogen NMR Relaxation Times and Relaxation Mechanisms from 1-100 MHz: Dependence on Tissue Type, NMR Frequency, Temperature, Species, Excision, and Age," *Medical Physics*, vol. 11, no. 4, pp. 425-448, July/August 1984.

19. E. McVeigh, M. Bronskill, and M. Henkelman, "Optimization of MR Protocols: A Statistical Decision Analysis Approach," *Magnetic Resonance in Medicine*, vol. 6, pp. 314-333, 1988.

20. P. Bottomley, C. Hardy, R. Argersinger, and G. Allen-Moore, "A Review of ^1H Nuclear Magnetic Resonance Relaxation in Pathology: Are T_1 and T_2 Diagnostic?," *Medical Physics*, vol. 14, pp. 1-37, Jan/Feb 1987.

21. G. Wright, D. Nishimura, and A. Macovski, "Flow-Independent Magnetic Resonance Projection Angiography," *Magnetic Resonance in Medicine*, vol. 17, no. 1, pp. 126-140, 1991.

22. R. Gronas, P. Kalman, A. Kiruluta, and G. Wright, "Protocol Optimization of Flow-Independent Angiography for Peripheral Vascular Disease," in *Third Meeting of the Society of Magnetic Resonance*, vol. 1, p. 75, August 1995.

23. J. Brittain, E. Olcott, A. Szuba, P. Irarrazabal, G. Gold, et al., "Improvements for Clinical 3D Flow-Independent Peripheral Angiography," in *Fourth Meeting of the Society of Magnetic Resonance*, vol. 1, p. 242, April 1996.

24. G. Wright, B. Hu, and A. Macovski, "Estimating Oxygen Saturation of Blood in Vivo with MRI at 1.5 T," *Journal of Magnetic Resonance Imaging*, pp. 275-283, 1991.

25. K. Li, G. Wright, L. Pelc, R. Dalman, J. Brittain, et al., "Oxygen Saturation of Blood in the Superior Mesenteric Vein: In Vivo Verification of MR Imaging Measurements in a Canine Model," *Radiology*, vol. 194, no. 2, pp. 321-326, 1995.

26. H. Nyquist, "Thermal Agitation of Electric Charge in Conductors," *Physical Review*, vol. 32, pp. 110-113, July 1928.

27. A. Macovski, "Noise in MRI," *Magnetic Resonance in Medicine*, vol. 36, no. 3, pp. 494-497, 1996.

28. W. Edelstein, G. Glover, C. Hardy, and R. Redington, "The Intrinsic Signal-To-Noise Ratio in NMR Imaging," *Magnetic Resonance in Medicine*, vol. 3, pp. 604-618, 1986.

29. M. Bronskill and M. Henkelman, "Artifacts in Magnetic Resonance Imaging," *Reviews of Magnetic Resonance in Medicine*, vol. 2, no. 1, 1987.

30. M. Wood and M. Henkelman, "MR Image Artifacts from Periodic Motion," *Medical Physics*, vol. 12, no. 2, pp. 143-151, 1985.

31. D. Bailes, D. Gilderdale, G. Bydder, A. Collins, and D. Firmin, "Respiratory Ordered Phase Encoding (ROPE): a Method for Reducing Respiratory Motion Artefacts in MR Imaging," *Journal of Computer Assisted Tomography*, pp. 835-838, 1985.

32. R. Ehman and J. Felmlee, "Adaptive Technique for High-Definition MR imaging of Moving Structures," *Radiology*, vol. 173, pp. 255-263, 1989.

33. M. Wood, M. Shivji, and P. Stanchev, "Planar-Motion Correction with Use of k-Space Data Acquired in Fourier MR Imaging," *Journal of Magnetic Resonance Imaging*, vol. 5, pp. 57-64, 1995.

34. T. Sachs, C. Meyer, P. Irarrazabal, B. Hu, D. Nishimura, and A. Macovski, "The Diminishing Variance Algorithm for Real-Time Reduction of Motion Artifacts in MRI," *Magnetic Resonance in Medicine*, vol. 34, pp. 412-422, 1995.

35. P.S. Melki, R.V. Mulkern, L.P. Panych, and F.A. Jolesz, "Comparing the FAISE Method with Conventional Dual-Echo Sequences," *Journal of Magnetic Resonance Imaging*, vol. 1, pp. 319-326, 1991.

36. H. Cline, W. Lorensen, R. Kikinis, and F. Jolesz, "Three-Dimensional Segmentation of MR Images of the Head Using Probability and Connectivity," *Journal of Computer Assisted Tomography*, vol. 14, no. 6, pp. 1037-1045, 1990.

37. J. Bezdek, L. Hall, and L. Clarke, "Review of MR Image Segmentation Techniques Using Pattern Recognition," *Medical Physics*, vol. 20, no. 4, pp. 1033-1048, 1993.

38. L. Clarke, R. Vethuizen, M. Camacho, J. Heine, M. Vaidyanathan, et al., "MRI Segmentation: Methods and Applications," *Magnetic Resonance Imaging*, vol. 13, no. 3, pp. 343-368, 1995.

39. W. Wells, W. Grimson, R. Kikinis, and F. Jolesz, "Adaptive Segmentation of MRI Data," *IEEE Transactions on Medical Imaging*, vol. 15, no. 4, pp. 429-445, 1996.

40. P. van den Elsen, E. Pol, and M. Viergever, "Medical Image Matching - a Review with Classification," *IEEE Engineering in Medicine and Biology*, vol. 12, pp. 26-39, 1993.

41. C. Meyer, G. Leichtman, J. Brunberg, R. Wahl, and L. Quint, "Simultaneous Usage of Homologous Points, Lines and Planes for Optimal, 3D, Linear Registration of Multimodality Imaging Data," *IEEE Transactions on Medical Imaging*, vol. 14, no. 1, pp. 1-11, 1995.

42. A. Kassam and M. Wood, "Fourier Registration of Three-Dimensional Brain MR Images: Exploiting the Axis of Rotation," *Journal of Magnetic Resonance Imaging*, vol. 6, no. 6, 1996. *In press.*

43. P. Thompson and A. Toga, "A Surface-Based Technique for Warping Three-Dimensional Images of the Brain," *IEEE Transactions on Medical Imaging*, vol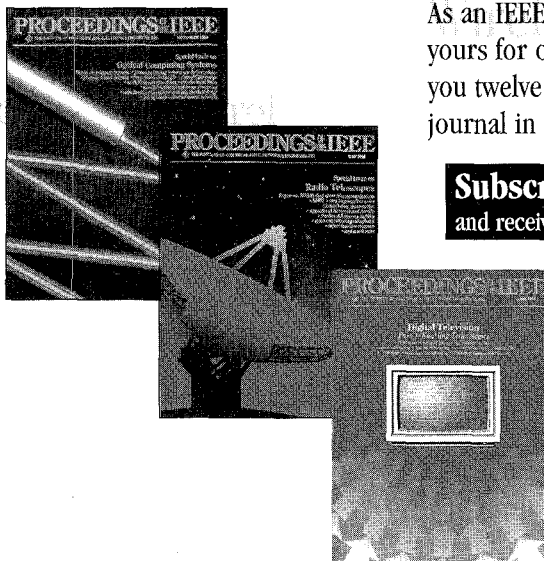. 15, no. 4, pp. 402-417, 1996.